

width than the one shown in Figure 2-14, allowing for appropriate sampling and signal digitisation by off-the-shelf data acquisition cards. In the interest of simulation playing time, in Figure 2-16, the mirror velocity is grossly exaggerated by at least a factor of 10,000x, as it would correspond to a 100 MHz A-line rate for a one-way pathlength scan range of 5 mm.

Figure 2-17 summarises key features of the low coherence interferometric process, where the coherence function is generated with increasing group delay by the increasingly uncorrelated temporal waveforms, *i.e.*, the one returning from the sample mirror and Doppler-shifted one, returning from the translating reference arm mirror.

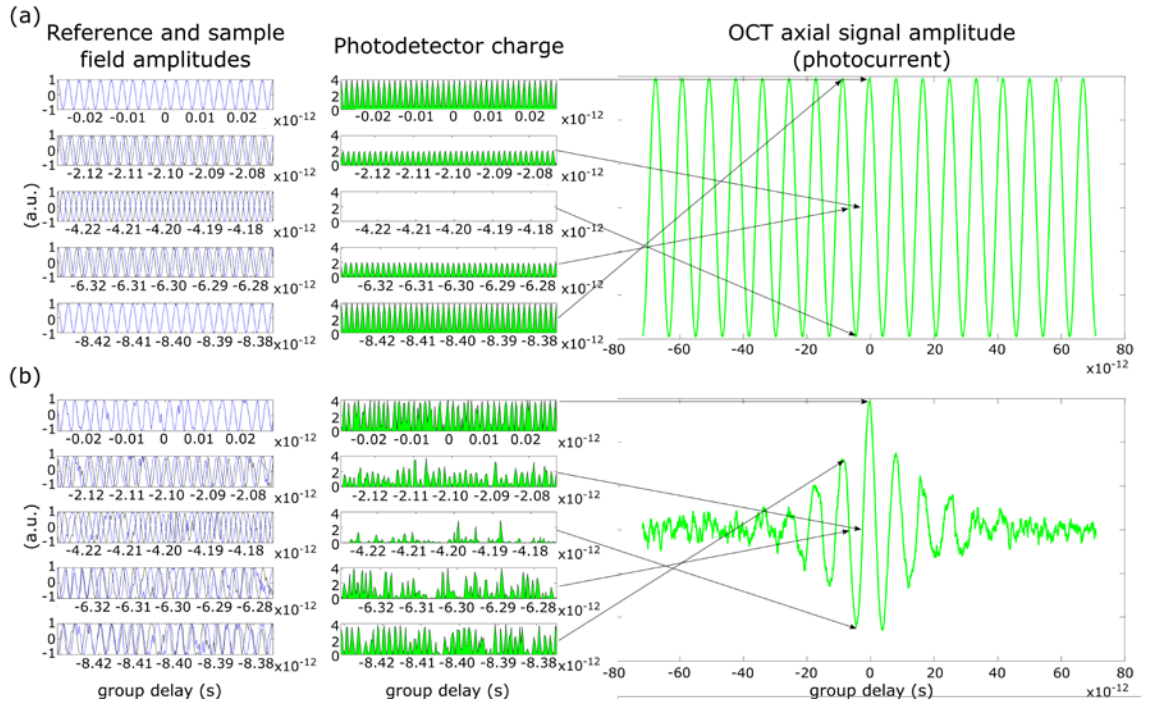


Figure 2-17. Field amplitudes (left panel), electric charge generated at the photodetector (middle panel) and detector photocurrent as a function of reference arm group delay. The delay is counted from the time the reference and sample arm mirror positions were matched. Representative steps in the generation of the OCT axial signal amplitude, *i.e.*, photocurrent, (a) with a monochromatic wave source and (b) with a polychromatic CW wave source. The close-ups in the left and middle panels are on five evenly spaced temporal windows within one period of the interferometric carrier (fringe).

Therefore, depth sectioning in TD-OCT can be achieved by scanning the position of the reference arm mirror, z_R [36]. An A-scan in TD-OCT, $I_D(\tau)$, is recorded as a function of time delay and then converted to depth, $I_D(z)$, where $z = \Delta L = v_g \tau_g$.

In general, the detected coherence function varies with both the group delay, $\tau_g(t)$, and the phase delay, $\tau_p(t)$ [36]. The coherence function can be expressed in terms of these delays as [36],

$$\gamma(\tau_g(t), \tau_p(t)) = |\gamma(\tau_g(t))| e^{-i(2\pi\nu_0\tau_p(t) + \alpha(t))} \quad (2-16)$$

where $\alpha(t)$ is a phase offset, accounting for phase modulations that may be either deliberately introduced, or arise as a result of fluctuations in ν_0 or shifts in path lengths as a result of mechanical jitter.

If the reference arm mirror is translated axially in air, then the group and phase delays are equal [36]. An additional phase delay can be introduced using a piezo-electric transducer [37], or the group and phase delays can be controlled separately by replacing the linear translation of the reference mirror by a frequency-domain optical delay line (FDODL) [36]. The detected intensity can then be expressed as [36],

$$I_D(\tau) = I_0 \left(R_s + R_R + 2\sqrt{R_s R_R} |\gamma(\tau_g(t))| \cos(2\pi f_0 \tau_p(t) + \alpha(t)) \right) \quad (2-17)$$

For most samples, the reflectance of the reference will be much greater than the reflectance of the sample, $R_R \gg R_s$, so the detected OCT signal is dominated by a constant signal background, R_R . This can be removed by high-pass filtering, leaving the desired signal from the sample, $\sqrt{R_s}$, amplified by the reference signal, $\sqrt{R_R}$, and modulated by a carrier, $\cos(2\pi f_0 \tau_p(t) + \alpha(t))$.

The earliest OCT systems were time-domain systems [10, 36, 37, 82, 83]. The principle advantage of TD-OCT is flexibility in the acquisition geometry, the absence of auto-correlation terms in the scan (see Section 2.1.3) and the absence of spectral roll-off of sensitivity with distance (see Section 2.1.3). OCT data can be acquired A-scan-first, by scanning the group delay, as in many early systems and in FD-OCT, but can also be acquired lateral scan first, by holding the group delay fixed and modulating $\alpha(t)$ whilst scanning laterally. This latter scenario is the acquisition geometry used for many full-field OCT and optical coherence microscopy (OCM) setups, which commonly use lenses with high numerical aperture (NA) to greatly increase their transverse resolution [38, 84]. The principle disadvantages of TD-OCT are that it suffers from low acquisition speed and sensitivity, and although the FDODL scanning mechanism allows for up to several kHz A-scan rate, it is still two or more orders of magnitude slower and subject to higher phase noise than FD-OCT A-scan rates [85].

2.1.3 Fourier-domain optical coherence tomography

Fourier-domain OCT systems represent the second generation of OCT systems [85], and operate on the principles of *spectral interferometry* [86]. Two implementations exist for FD-OCT: spectral-domain OCT (SD-OCT) [85] uses broad-band light as the source and a

spectrometer as the detector; and swept-source OCT (SS-OCT) or optical frequency-domain imaging (OFDI) [87-89] uses a frequency swept-laser as the source, and records the output using a photodiode as the detector. Advantages of these implementations over TD-OCT are the much faster acquisition speeds [85, 90, 91] and higher sensitivity (see Section 2.3.2).

Spectrometer and swept sources record or produce an output signal, which is, spatially or temporally, respectively, nearly linear with wavelength. Designs linear in wavenumber can also be realised in hardware. Nevertheless, in FD-OCT, with appropriate calibration A-scans are computed as a function of wavenumber, k [10], with the reference mirror held stationary, as in Figure 2-8(b)

$$I_D(k) = W_s(k) \otimes \overline{|E_s(k) + E_R(k)|^2}, \quad (2-18)$$

where $W_s(k)$ is a function describing the sampling of wavenumbers by the finite pixel size of the spectrometer (SD-OCT) or of the finite line-width of the swept-source (SS-OCT), and \otimes is the convolution operator.

Assuming the sample is made up of reflectors spaced far enough to avoid near-field interactions, and neglecting dispersion, the fields reflected from the (stationary) reference mirror and from the n reflectors in the sample arm are, respectively:

$$E_R(k) \propto \sqrt{g(k)} \sqrt{R_R} e^{i\phi_R(k)}, \quad (2-19)$$

$$E_s(k) \propto \sqrt{g(k)} \sqrt{R_s} e^{i\phi_s(k)} = \sqrt{g(k)} \sum_n \sqrt{R_{s_n}} e^{i\phi_{s_n}(k)}, \quad (2-20)$$

where, $g(k)$ is the normalised power spectral density of the light source as a function of wavenumber. $\phi_R(k) = 2kz_R$ and $\phi_{s_n}(k) = 2kz_{s_n}$ are the phase responses of the reference arm and of the sample arm, at $z = z_R$ and at the individual sample reflectors positions $z = z_{s_n}$, respectively. Therefore, the detected irradiance can be expressed as [82],

$$\begin{aligned} I_D(k) &\propto W_s(k) \otimes \overline{|E_s(k)|^2 + |E_R(k)|^2 + 2\text{Re}\{E_s^*(k)E_R(k)\}} = \\ &= W_s(k) \otimes g(k) \left[R_s(k) + R_R(k) + 2\sqrt{R_s(k)R_R} \text{Re}\{e^{i\phi_R(k)-i\phi_s(k)}\} \right] = \\ &= W_s(k) \otimes g(k) \left[\sum_n R_{s_n}(k) + R_R(k) + 2 \sum_n \sqrt{R_{s_n}(k)R_R(k)} \text{Re}\{e^{i2k(z_R-z_{s_n})}\} \right. \\ &\quad \left. + 2 \sum_{n \neq m} \sqrt{R_{s_m}(k)R_{s_n}(k)} \text{Re}\{e^{i2k(z_{s_n}-z_{s_m})}\} \right]. \end{aligned} \quad (2-21)$$

A depth-resolved A-scan is then obtained through inverse Fourier transform of $I_D(k)$. Using the properties of the Fourier Transform that $\frac{1}{2}[\delta(z+z_0) + \delta(z-z_0)]$

$\overset{\mathcal{F}}{\leftrightarrow} \text{Re}\{e^{ikz_0}\}$, $x(z) \otimes y(z) \overset{\mathcal{F}}{\leftrightarrow} X(k)Y(k)$, and $x(z)y(z) \overset{\mathcal{F}}{\leftrightarrow} X(k) \otimes Y(k)$, the depth-resolved A-scan, $i_D(z)$, simplifies to [82],

$$i_D(z) \propto \Psi(z) \otimes w_s(z) \left[\begin{aligned} & \left(\sum_n R_{s_n} + R_R \right) \delta(z) \\ & + \sum_n \sqrt{R_{s_n} R_R} \delta(z \pm 2(z_R - z_{s_n})) \\ & + \frac{1}{2} \sum_{n \neq m} \sqrt{R_{s_m} R_{s_n}} \delta(z \pm 2(z_{s_n} - z_{s_m})) \end{aligned} \right], \quad (2-22)$$

where $\Psi(z)$ is an effective axial point-spread-function due to the source bandwidth, and $w_s(z)$ causes the system sensitivity to drop with distance from the zero delay due to the band-limited shape of the Fourier transform of the wavenumber sampling function, determined by the pixel size or source linewidth, and is often referred to as *spectral roll-off*. The components of Eq. (2-22) are illustrated in Figure 2-18.

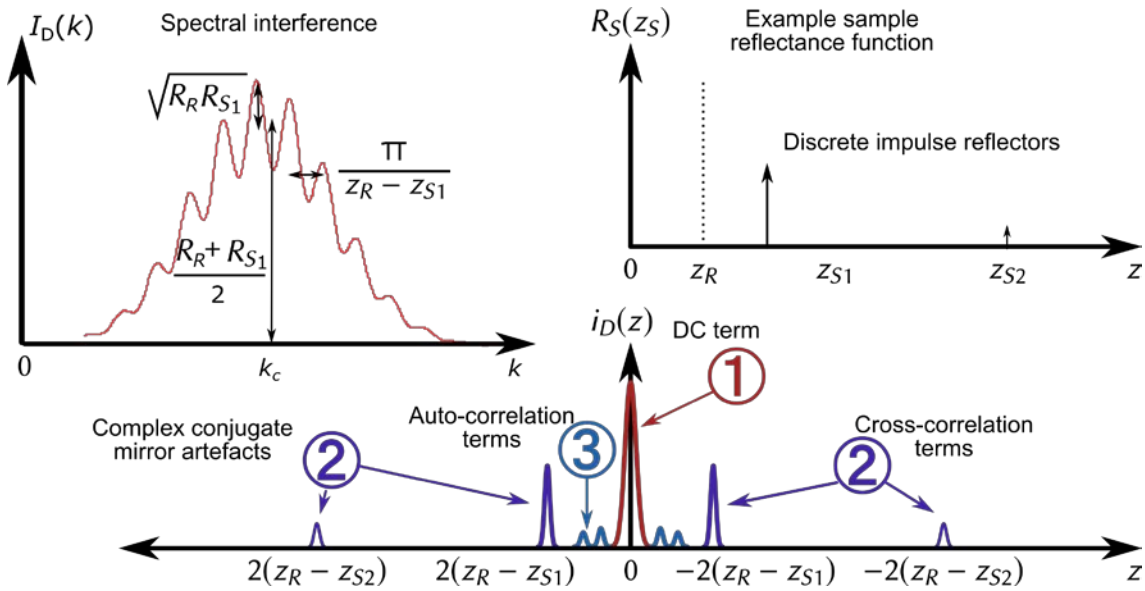


Figure 2-18. An example of the spectral interference generated by a discrete sample reflectivity function (top), and the corresponding A-scan captured by FD-OCT (bottom). The sample reflectivity function can be written as $R_s(z_s) = \sum_n \delta(z_s - z_{s_n})$. 1: DC term; 2: Cross-correlation terms; 3: auto-correlation terms, corresponding to the three terms in Eq. (2-22). Adapted from [82].

Once again, for most samples $R_R \gg R_s$, so the recorded signal tends to be dominated by the DC term. The cross-correlation terms represent the desired signal proportional to the square root of the sample reflectances. The auto-correlation terms can create “ghost” images, and, as such, represent unwanted noise in the signal, but are usually much smaller than the other terms.

The reconstructed spatial signal, $i_D(z)$, is mirrored about $z = 0$, and about the maximum z -depth, $z = z_{max}$. This is because only the real part of the spectral interferogram, $I_D(k)$, is typically recorded, so its Fourier transform presents an ambiguity with respect to the zero delay [92]. That is, a reflector at $z_s = z_R - z_1$, or $z_s = z_R + z_{max} - z_1$ will both appear as complex conjugate mirror artefacts at $z = z_1$. Recording additional A-scans with variable phase shifts in the reference arm resolves these mirror artefacts and enables reconstruction of the full complex spectral interferogram [92]. In practice, however, the attenuation of most soft tissues reduces any signal from beyond z_{max} to below the sensitivity limit, and the overlap between auto- and cross-correlation terms can be minimized by adjusting the relative positions of the sample and reference. It is, thus, more common to simply discard the negative z components of $i_D(z)$ [85]. In FD-OCT, $I_D(k)$ is fully real and $i_D(z)$ is a complex quantity. Thus, unlike TD-OCT, FD-OCT directly provides access to the depth-resolved phase of the backscattered light, as well as the irradiance [92]. The phase information is coarsely subsampled in the vast majority of cases, yet, relative phase measurements provide additional information that has been exploited in Doppler OCT and the emerging field of optical coherence elastography (OCE) that is a major topic of this thesis. This topic is treated in more detail in the following section.

2.2 Optical coherence elastography

Key to the advancement of the optical microscopy of tissue has been the exploration of sources of contrast aimed at improving the visualization of structure and providing information on function. On length scales from the molecular (sub-nanometre) to many millimetres, elastic scattering is a source of contrast that provides information on structure, size and motion of tissue constituents [44], and spectroscopy provides information on molecular composition [93]. Over the same length scales, the mechanical properties of tissue are a rich alternative to optical sources of contrast [94]. Such properties govern the mechanical interactions between cells and their environment, which, in concert with chemical interactions, determine how they grow, differentiate and migrate. The impairment of a cell's capacity to respond to mechanical forces contributes to the pathogenesis of diseases such as cancer [20], and leads to differences in the mechanical properties of normal and malignant tissue. Tumour cells are known to be commonly softer than their normal counterparts and, at the same time, tumours commonly cause the generation of additional collagen-dense stroma, making them feel stiffer on the macro-scale [19]. The

result of this innate heterogeneity is that, on the microscopic scale, malignant tissues often have a broader stiffness distribution than normal tissues [19].

The measurement of the mechanical properties of cells and tissues on the nano- and micro-scale, using techniques such as atomic force microscopy [19] and optical tweezers [95], has contributed greatly to our understanding of the role of mechanical interactions in disease. On the macro-scale, physicians have used palpation as a means of diagnosis for centuries. The advent of medical imaging, such as ultrasound and magnetic resonance imaging, has provided the means for the development of elastography, the use of imaging to map mechanical properties [16, 96, 97]. In elastography, the tissue is mechanically loaded and imaged to measure its deformation. For the class of methods based on compressive loading, the vector field of displacements between acquired images is used to estimate components of the local strain tensor (change in length per unit length), which are displayed in images (elastograms) that represent relative tissue stiffness [16]. Elastography has a more-than-twenty-year history [98] during which many loading methods and means of extracting mechanical properties have been explored, and clinical applications have emerged, e.g., in breast cancer [17] and liver fibrosis [99].

Amongst optical elastography methods [22, 100, 101], the use of optical coherence tomography (OCT) to measure displacement, termed optical coherence elastography (OCE), has been the most prominent [18, 22, 102-110].

2.2.1 Elasticity

Sample elasticity and deformation can be described using the formalisms of continuum mechanics [111]. The applied load, and the resulting deformation, are described in terms of stress and strain tensors. Elasticity is then defined by the constitutive equation that links these tensors.

The local stress acting at point P in a deformable body, in an infinitesimally small cubic volume about the point P, is defined as the resultant force acting on one of the infinitesimal cube facets, ΔA , over the area of ΔA . It is in units of Pascals, and equivalent to force per unit area N/m^2 . It can be decomposed into components orthogonal to the surface ΔA (*normal stress*) and parallel to it (*shear stresses*). The local strain along one direction (*normal strain*) is defined as the change in length of the infinitesimal cube edge aligned with that direction over the original length. Strain in a plane (*sheer strain*) is related to the change in angle between two edges of the infinitesimal cube that were originally orthogonal. As strain is a ratio of lengths, it is unitless.

If we consider the relationship between stress and strain to be linear and constant with time, *i.e.*, the sample is modelled as being a linearly elastic solid, the constitutive equation is given by

$$\sigma_{ij} = \sum_{k=1}^3 \sum_{l=1}^3 C_{ijkl} \varepsilon_{kl} , \quad (2-23)$$

where σ_{ij} and ε_{kl} are elements of the stress and strain tensors, respectively, and C_{ijkl} refers to elements of the elasticity tensor, a 4-th order tensor with $3 \times 3 \times 3 \times 3 = 81$ components. If the sample's mechanical properties are independent of direction, *i.e.*, isotropic, the constitutive equation simplifies to

$$\sigma_{ij} = \lambda \sum_k \varepsilon_k \delta_{ij} + 2\mu \varepsilon_{ij} , \quad (2-24)$$

where $\varepsilon_k = \varepsilon_{kk}$ are the normal strain components, δ_{ij} is the Kronecker delta function ($\delta_{ij} = 1$ if $i = j$, and 0 otherwise), and λ and μ are called the Lamé coefficients, in units of Pascals, that describe the sample's mechanical properties.

Four descriptors can be derived from the Lamé coefficients: Young's modulus, Poisson's ratio, shear modulus, and bulk modulus [111].

Young's modulus, E , is the ratio of uniaxial stress, σ_i , to the resulting uniaxial strain, ε_i , where the index i represents any of the coordinate directions. For example, for a load acting along the z -axis,

$$E = \frac{\sigma_z}{\varepsilon_z} . \quad (2-25)$$

In terms of the Lamé coefficients, $E = \mu(3\lambda + 2\mu)/(\lambda + \mu)$. Since strain is unitless, Young's modulus is in units of Pascals, the same as stress.

Poisson's ratio, ν , is defined as the ratio of transverse to axial strain. For a sample under compression, it is the ratio of lateral expansion to axial compression. For a sample under tension, it is the ratio of lateral compression to axial extension. For example, for a load acting along the z -axis,

$$\nu = -\frac{\varepsilon_x}{\varepsilon_z} = -\frac{\varepsilon_y}{\varepsilon_z} . \quad (2-26)$$

In terms of the Lamé coefficients, $\nu = \lambda/2(\lambda + \mu)$. As a ratio of strains, Poisson's ratio is unitless. For most materials, $0 < \nu < 0.5$.

Shear modulus, G , is the ratio of an applied shear stress to the resulting shear strain. For example, for a shear load applied parallel to the xz -plane,

$$G = \frac{\sigma_{xz}}{\varepsilon_{xz}}. \quad (2-27)$$

Shear modulus is equal to the Lamé coefficient μ , and is in units of Pascals. It can alternatively be expressed in terms of Young's modulus and Poisson's ratio as $G = E/2(1 + \nu)$.

Bulk modulus, K , is a measure of a sample's resistance to uniform compression. It is defined as the ratio of the hydrostatic pressure, σ , to the resulting unit change in volume, $\Delta V/V$,

$$K = -\frac{\sigma}{\Delta V/V}. \quad (2-28)$$

Hydrostatic pressure describes the case where all the normal stress components are equal, $\sigma = \sigma_x = \sigma_y = \sigma_z$ and all shear stresses are zero. In terms of the Lamé coefficients, $K = \lambda + 2\mu/3$. Bulk modulus is in units of Pascals.

When dynamic loading is used, the solution to the constitutive equation for a linear elastic solid in motion (Navier's equation) gives rise to waves that propagate through the material at speeds dependent on the mechanical properties. A load applied orthogonally to the surface of the sample generates surface waves, called surface acoustic waves (SAW) in elastography. Rayleigh waves, containing both longitudinal and vertical shear components [112], are a good model for SAW. The load also creates waves within the bulk of the material. Both longitudinal (pressure) and transverse (shear) waves are generated and can propagate independently [111]. The phase velocities of SAWs, c_p [113], longitudinal waves, c_l [111], and shear waves (SW), c_s [111], are given by, respectively,

$$c_p = \frac{0.87+1.12\nu}{1+\nu} \sqrt{\frac{\mu}{\rho}}, \quad c_l = \sqrt{\frac{\lambda+2\mu}{\rho}}, \quad \text{and} \quad c_s = \sqrt{\frac{\mu}{\rho}}, \quad (2-29)$$

where ρ is the material density. The SAW phase velocity, c_p , is related to the real root of the Rayleigh wave equation [112, 114], $\eta^6 - 8\eta^4 + 8(3 - 2\xi^2)\eta^2 - 16(1 - \xi^2) = 0$, where $\eta = c_p/c_s$ and $\xi = c_s/c_l$. In case of Poisson's ratios in the range $0 < \nu < 0.5$, as in most biomaterials [112], an approximate solution is given by $\eta = (0.87 + 1.12\nu)/(1 + \nu)$, which yields the expression for the SAW phase velocity shown in Eq. (2-29) [114].

Only two of the previous quantities are needed to fully specify the material's mechanical properties, as they all linearly depend on the Lamé coefficients.

The usual goal in OCE is to measure Young's modulus, E , shear modulus, G , SAW velocity, c_p , or SW velocity, c_s (although SAW and SW velocity require knowledge of the

sample density) [18], since Poisson's ratio, ν , and the bulk modulus, K , do not vary greatly between tissues, and the longitudinal wave velocity, c_l , is typically too fast to measure with OCE [98]. In fact, the Poisson's ratio of most soft tissues is close to (but never greater than) 0.5. This is due to the high water content of soft tissue making tissue effectively incompressible. Soft tissues also generally possess a bulk modulus, K , very close to that of water [16]. For typical biomaterials, the velocity of pressure waves, c_l , is orders of magnitude faster than that of shear waves, c_s , typically in the order of 1000s of m/s, and m/s, respectively.

In soft tissue, Young's modulus has the highest dynamic range compared to the shear modulus, the SAW velocity, and the SW velocity. In fact, under the assumption that $\nu \approx 0.5$, it can be shown that $E \approx 3G$, $E \propto c_p^2$, and $E \propto c_s^2$. Therefore the most commonly probed property in OCE to characterise tissue elasticity is Young's modulus [18].

Elasticity of tissue

Tissue elasticity is determined by both its constituent materials and the structural arrangement of these constituents [115]. There are several types of tissue constituents: cellular, *e.g.*, adipose, blood, and epithelial cells; polymer, *e.g.*, collagen; elastomer, *e.g.*, elastin; or ceramic, *e.g.*, dentin and enamel [115]. The density of these constituents partially determines tissue elasticity, with higher densities related to stiffer tissues with higher Young's modulus [116]. The arrangement of these tissue constituents, from the nanometre scale (molecular level) to the centimetre scale (organ level) in a hierarchy of structures (linked to their function), is also an important factor in determining tissue elasticity [115]. Tissue structure and, consequently, the measured elasticity can vary greatly depending on the scale being probed (cellular, micro, or organ scale). A study of the elasticity of porcine cartilage by Stolz *et al.* [117] showed a 100-fold lower Young's modulus at the nanometre-scale ($\sim 20\text{--}50$ kPa) compared to the micrometre-scale (~ 2.6 MPa), highlighting the importance of scale as well as structure in determining tissue mechanical properties. Figure 2-19 illustrates graphically the Young's modulus of various tissues constituents, structures and whole organs.

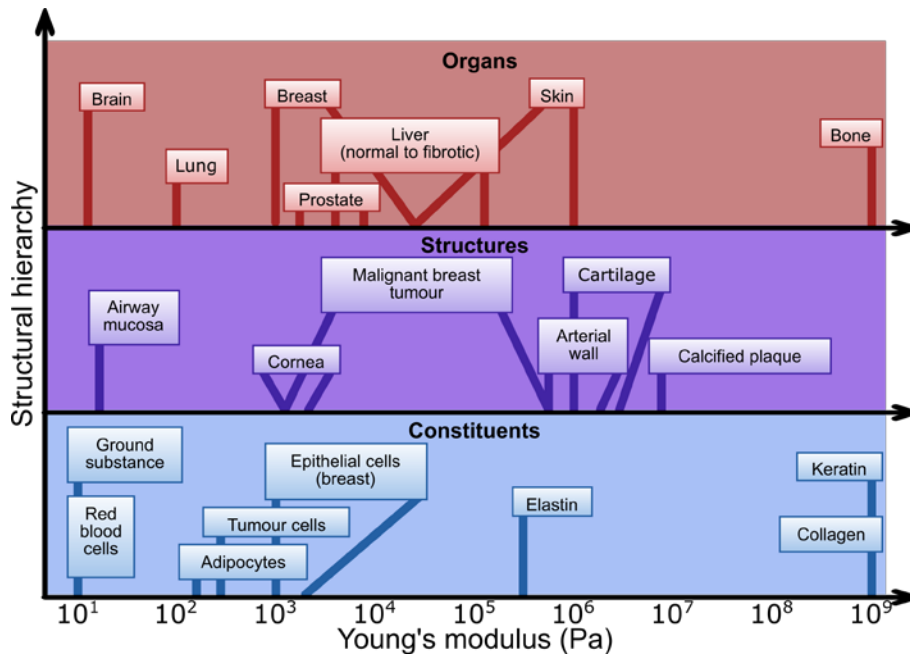


Figure 2-19. Reported values and ranges of Young's modulus for selected tissues and tissue constituents. Adapted from [18].

The figure shows that the Young's modulus of tissue spans more than eight orders of magnitude, showing high contrast potential for elastography.

Many diseases are correlated with a modification of tissue constituents and hierarchical structure. The mechanical properties of diseased tissue vary from those of its healthy counterpart, and they vary differently at different scales. A complex, two-way interplay between tissue mechanics and disease genesis and progression is revealed by studies in bio-mechanics using cellular/sub-cellular methods, such as atomic force microscopy (AFM), optical tweezers, traction-force microscopy, and micropipette aspiration [118-120].

OCE can currently probe the elasticity of tissues on the intermediate scale (10s-100s μm) between that of cells and whole organs, and has the potential to aid in the understanding, diagnosis, and assessment of treatments of conditions and diseases [18, 105]. There is a wealth of applications where OCE has already shown potential to measure tissue mechanical properties: *e.g.*, in dermatology [104, 121-126], in eye diseases [127-130], in lung diseases [131, 132], and in breast tissue [133]. Similarly, in cardiovascular disease, OCE could aid in measuring the mechanical properties of atherosclerotic plaques [134-136], which are likely to play a role in plaque rupture [136, 137]. In cancer, assessment of tumour margins may benefit from the high resolution and sensitivity to tumour detection of OCE. Also, the field of biomechanics would greatly benefit from an *in situ* high resolution OCE system, capable of measuring cellular-resolution mechanical properties of tissue in its native environment in 3-D and at depth below the tissue surface. In this thesis, we propose and demonstrate such system in Chapter 7.

2.2.2 Principles of optical coherence elastography

Many different OCE techniques have been developed and implemented to date [18, 105]. OCT is the underlying imaging modality for all these techniques, but they vary in the way they estimate displacement from the OCT scan and/or the mechanism used to load the tissue. In each technique, a mechanical model of deformation is then used to estimate a tissue mechanical property, which is mapped into an elastogram.

The two primary methods of measuring tissue deformation are based on speckle tracking (see Section 2.3.3) and phase-sensitive detection [18]. Selected performance parameters for these mechanisms are listed in Table 2-1. The two most commonly used loading mechanisms are based on uniaxial compression, and pulsed or periodic actuation (contact or non-contact) generating elastic waves in the sample [18]. Selected performance parameters for these mechanisms are listed in Table 2-2.

Table 2-1. Imaging parameters for OCE displacement estimation methods. Adapted from [18].

	Speckle tracking	Phase-sensitive
Displacement		
Minimum	$\sim 0.5 \times \text{voxel size}$	$\sim 20 \text{ pm}^*$
Maximum	$\sim 0.5 \times \text{OCT resolution}$	$\sim \text{source wavelength (without phase unwrapping)}$ $\sim 5 \times \text{source wavelength (with phase unwrapping)}$
Resolution		
Axial	$\sim 5 - 10 \times \text{OCT resolution}$	Same as OCT
Transverse	$\sim 5 - 10 \times \text{OCT resolution}$	Same as OCT
Mapping of elasticity tensor in	3-D	1-D

* Method combines multiple A-scans for each measurement [138].

Table 2-2. Experimental and theoretical imaging parameters for OCE loading methods. Adapted from [18].

	Compression	Elastic wave	
		Surface acoustic	Shear
Measured parameter	Local strain ϵ_l	Phase velocity, c_p	Phase velocity, c_s
Dynamic range*	~ 660 ($1.6 \text{ m}\epsilon / \sim 2.4 \text{ }\mu\epsilon$) [139]	~ 450 ($5 \text{ m/s} / \sim 11 \text{ mm/s}$) [107]	14 ($7 \text{ m/s} / 0.5 \text{ m/s}$) [140]
Quantitative	N	Y (density knowledge required)	Y (density knowledge required)
Axial resolution	40-120 μm [106]	Unknown	Unknown
Transverse resolution	Same as OCT	500-1000 μm	500 μm
Loading frequency	0 - 800 Hz [141]	0 - ~ 300 Hz [101]	1 - 5 kHz [140]

* Reported max/min of measured parameter

Displacement estimation

In this thesis, we focus on phase-sensitive OCE. In phase-sensitive OCE, the axial displacement within a sample in response to a load, $d(x, y, z)$, is calculated from the change in the OCT phase, $\Delta\phi(x, y, z)$, between scans of the loaded and unloaded sample [103, 106, 142], *i.e.*,

$$d(x, y, z) = \frac{\lambda_0}{4\pi n} \Delta\phi(x, y, z), \quad (2-30)$$

where λ_0 is the mean free-space wavelength of the OCT system, and n is the sample refractive index at location (x, y, z) . In compression OCE, the axial displacement can be used to calculate the local axial strain (*i.e.*, the strain defined over a finite range) [103, 106, 142] and in shear wave and surface acoustic wave OCE, it can be used to calculate the phase velocity of the propagating wave [107, 143-145].

Loading mechanism

In this thesis, we focus on compression OCE. This technique requires only two OCT scans: one of the sample unloaded, or under a static preload, and another of the sample under an additional compressive load described by an applied stress tensor, σ [18]. The resulting sample deformation can be quantified by the strain tensor, ε [18].

The compressive load is applied by an actuator over an area bigger than the transverse field of view, but ideally just big enough to avoid edge effects being visible in the image. As tissues are intrinsically non-linearly elastic, the initial preload the sample is subjected to, in order to flatten out its uneven surface morphology and ensure contact with the compression actuator, is very important. For induced strains < 0.1 , it has been reported that tissues such as breast and prostate, and elastomers such as silicone, can be described by a linear elastic model [24, 29, 146]. Additionally, considering the sample to be isotropic, if the compressive load is uniform and uniaxial at the sample surface, then the uniaxial stress, σ_z , and strain, ε_z , of the sample are related through a single constant, Young's modulus, $E = \sigma_z / \varepsilon_z$, which is a common measure of material stiffness. In general, the Young's modulus will vary throughout the sample, and a map of Young's modulus can be calculated by measuring the local strains and stresses within the sample.

Elastogram generation

The local strain can be determined from the spatial derivative of the measured displacement at each point within the sample. It is not straightforward, however, to

measure the local stress distributed throughout the material, although our group has recently proposed a technique to measure local stress at the tissue surface [147]. Compression elastograms are typically, thus, a map of the strain distribution throughout the sample in response to the load.

Phase-sensitive detection generally measures only the axial displacement, so the local, axial strain, $\varepsilon_z(x, y, z)$, in phase-sensitive compression OCE is calculated as

$$\varepsilon_z(x, y, z) = \frac{\Delta d(x, y, z)}{\Delta z}, \quad (2-31)$$

where $\Delta d(x, y, z)$ is the change in axial displacement over the depth range Δz . In this thesis, the phase difference, $\Delta\phi(x, y, z)$, is unwrapped prior to calculating the axial displacement to increase the measurable dynamic range [24].

The axial strain is then calculated using weighted-least-squares (WLS) linear regression over a sliding window on the axial displacement, with the weights being the OCT signal-to-noise ratio associated with each displacement measurement [106].

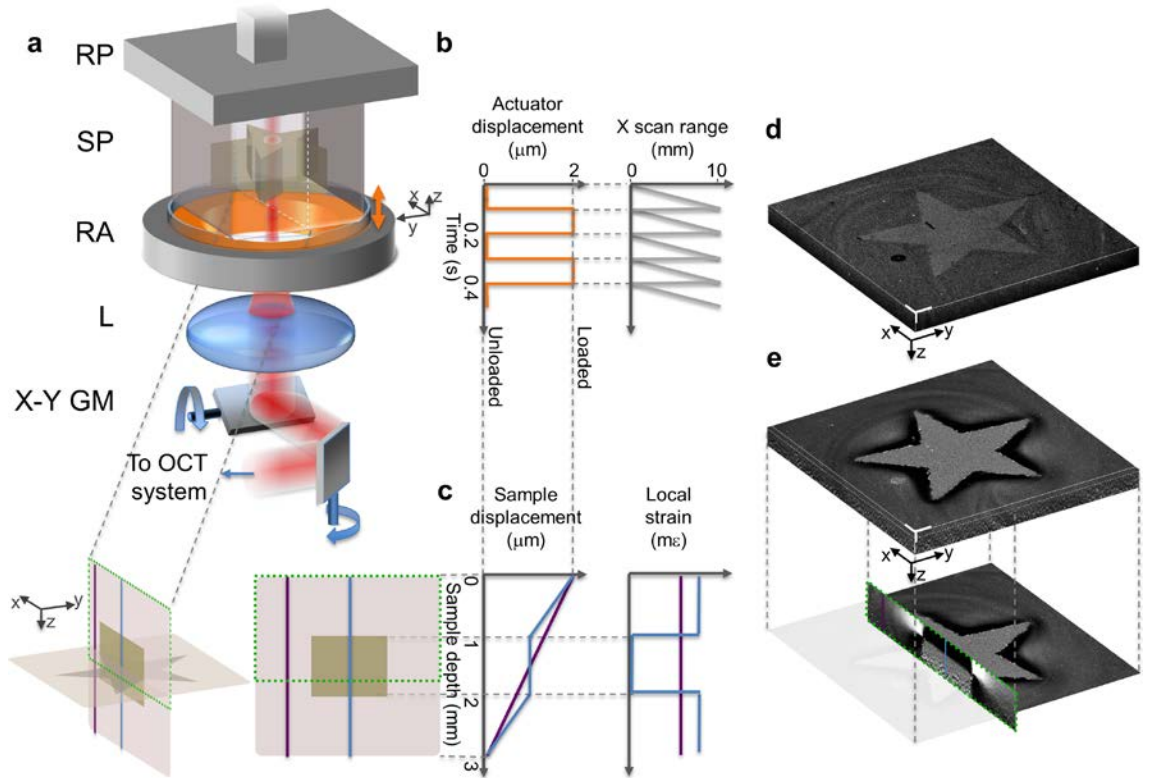


Figure 2-20. Illustration of phase-sensitive compression optical coherence elastography on a structured phantom. (a) Sample arm of the imaging system. RP, rigid plate; SP, structured phantom; RA, ring actuator and window; L, Lens; X-Y GM, xy -scanning galvanometer mirrors. Perspective and side-view illustrations of the phantom containing a rigid star-shaped inclusion are also shown. (b) Displacement of the ring actuator and synchronised x -scanning galvanometer mirror scan pattern. (c) Illustrations of displacement and local strain at two locations in the phantom. (d) Three-dimensional OCT perspective view of the phantom. (e) Corresponding perspective view of the three-dimensional elastogram displaying the local strain, and a cutaway view revealing a B-mode elastogram through the central region of the inclusion. Scale bars, 0.5 mm. Adapted from [24].

Figure 2-20 illustrates the process of the loading mechanism and elastogram generation for phase-sensitive compression OCE. The sample is a silicone phantom containing a rigid star-shaped inclusion, as described in Section 4.7.

Figure 2-21 shows the capabilities of OCE in differentiating malignant and healthy breast tissue in a freshly excised breast sample, based on the mechanical properties of these tissues.

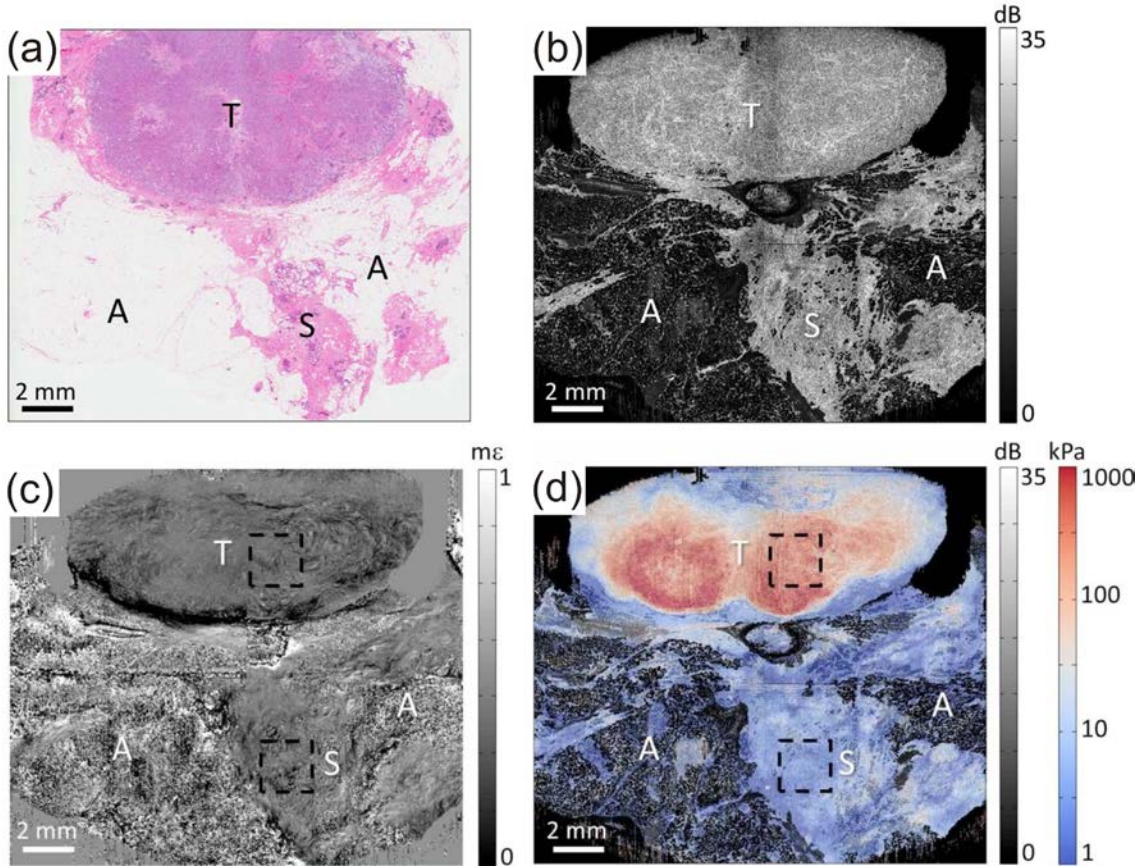


Figure 2-21. Optical coherence elastography of a malignant breast tumour with quantitative elasticity estimation. (a) Haematoxylin and eosin (H&E) histology. (b) *En-face* OCT image. (c) *En-face* strain elastogram. (d) Fused *en-face* OCT and quantitative optical coherence elastography. Elasticity is plotted on a logarithmic scale. A = adipose, S = stroma, T = tumour. Dashed boxes indicate regions over which mean strain and elasticity values were calculated. In the strain image, this ratio is 0.77, and in the elasticity image it is 82, *i.e.*, the tumour is much stiffer than the healthy stroma and as a result it strains less under compression. Adapted from [148].

2.3 Image quality

OCT image quality is defined by many descriptors, such as resolution (axial and transverse), depth of field (DOF), signal-to-noise ratio, sensitivity, contrast, and speckle contrast. Improvement of all these descriptors at once is unfeasible, as many are in a trade-off relationship with one another. In the following, we shall describe each one and the existing trade-off relationships. We shall also define the noise sources affecting elastogram image quality.

2.3.1 OCT resolution and depth of field

Unlike most optical microscopies, such as confocal microscopy, the axial and transverse resolution in OCT are determined by separate, decoupled, processes.

Axial resolution

The axial resolution is determined by the coherence function of the light source [11, 36]; which is sometimes referred to as the *coherence gate*. Often the light source will have a power spectral density that differs from a Gaussian function. Nevertheless, a Gaussian power spectral density is sought after, as it provides the smallest time-bandwidth product, *i.e.*, its coherence gate is the smallest for a given spectral (frequency) bandwidth [33]. With FD-OCT spectral reshaping to a Gaussian power spectral density is possible in post-processing. If we consider a light source with a Gaussian power spectral density, as in Eq. (2-11), and we express the coherence function, Eq. (2-12), as a function of the physical pathlength z within a sample of group refractive index n_g , we obtain the axial point-spread-function (PSF) (for further details see Section 5.2.1):

$$\Psi(z) \triangleq e^{-\left(\frac{\pi \Delta\lambda}{\sqrt{\ln 2} \lambda_0^2} n_g z\right)^2} e^{-i\frac{2\pi}{\lambda}(2n_g z)}, \quad (2-32)$$

where λ_0 is the centre wavelength of the source, and $\Delta\lambda$ is the full-width-at-half-maximum (FWHM) spectral bandwidth. The axial resolution, Δz_{FWHM} , is typically defined as the FWHM of the intensity of the axial PSF. For a Gaussian source spectrum, this corresponds to [36, 92]

$$\Delta z_{FWHM} = \frac{2 \ln 2}{\pi} \frac{\lambda_0^2}{\Delta\lambda n_g}. \quad (2-33)$$

Thus, improving the axial resolution in OCT requires greater source bandwidths and/or shorter source wavelengths.

Transverse resolution

The transverse resolution is entirely dependent on the sample arm optics, as in most other microscopies. There are several criteria to determine the minimum transverse distance that two point-source objects have to be separated by, in order to distinguish the two sources from each other. Excluding super-resolution techniques, all light microscopies have their optimum transverse resolution bound by the limit of diffraction, as illustrated in Figure 2-21. When overfilling the objective lens, as in confocal microscopy, an Airy diffraction

pattern is generated as the transverse profile in focus. [149]. The bigger the objective aperture, the smaller the central Airy disk radius $r = 1.22\lambda/2NA$, where the lens numerical aperture is $NA = n_p \sin\theta$.

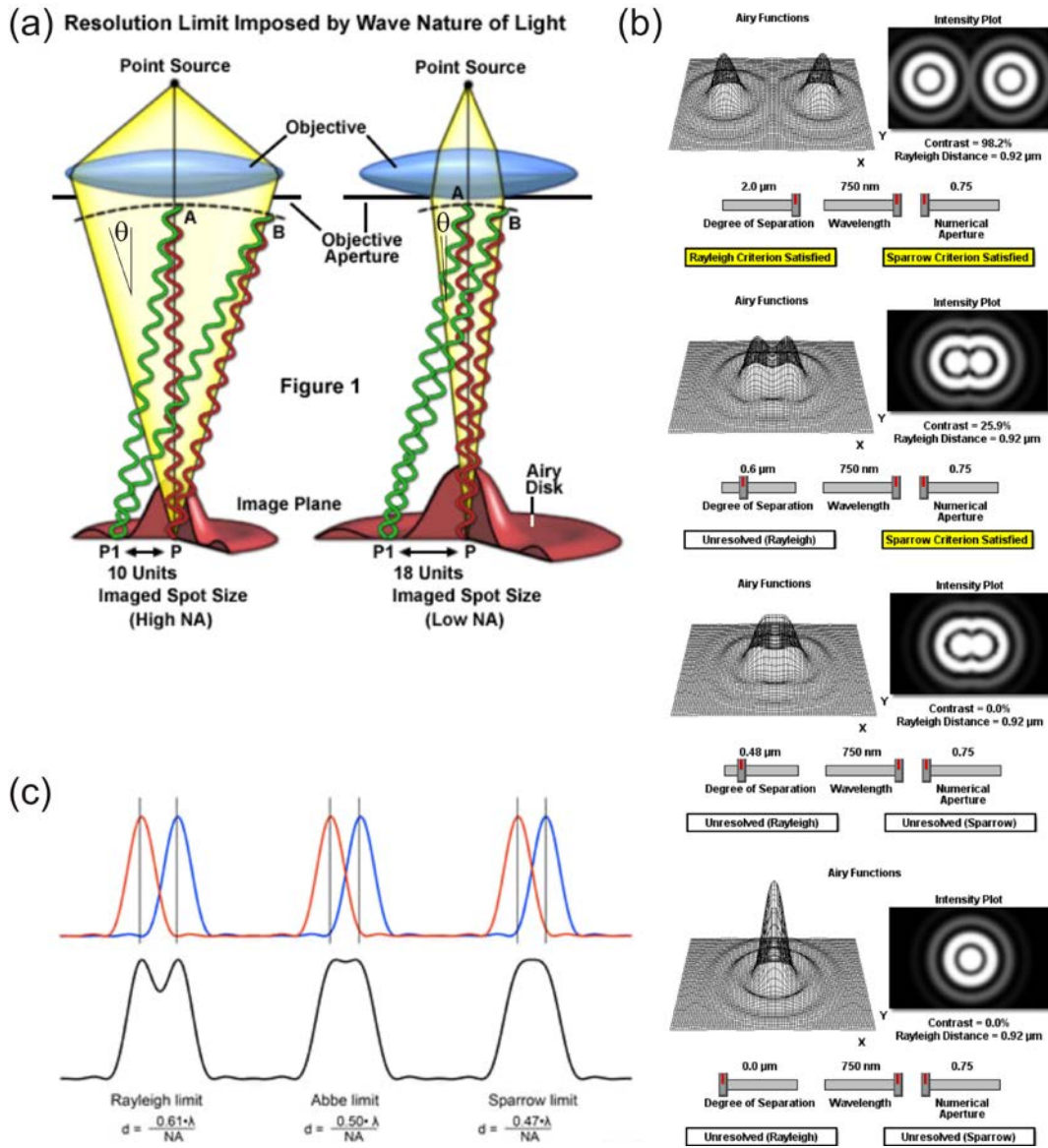


Figure 2-22. Schematic illustrating diffraction-limited resolution in microscopy. (a) Transverse resolution depends linearly on the numerical aperture, *i.e.*, the size of the Airy disk diffraction pattern in the transverse plane in focus is smaller for higher NA. (b) Illustration of the signal from two point sources as a function of their separation. (c) Three criteria for transverse resolution, using overfilled objective lenses. Adapted from [150-152].

The Rayleigh criterion for resolution is satisfied when the principal diffraction maximum (the central spot of the Airy disk) from the image of one of the point sources overlaps with the first minimum (dark region surrounding the central spot) of the Airy disk from the other point source. The Abbe criterion is less stringent and, when satisfied, a small dip is still discernible between the two maxima. In the Sparrow criterion, the sum of the two Airy patterns produces a flat intensity profile.

In OCT, the lens aperture is seldom overfilled, so Gaussian beam optics [153] is used to determine the axial and transverse beam profile, and the corresponding PSF. Assuming a collimated Gaussian beam with $1/e^2$ of intensity radius ω_0' , and a sample objective lens with focal length f , then the beam numerical aperture is $NA \cong \omega_0'/f$ [36] and the transverse resolution at the focal plane, defined as the FWHM of the transverse PSF, Δx_{FWHM} , (see Section 5.4.1) is [82]

$$\begin{aligned} \Delta x_{FWHM_{PSF}} &= \sqrt{\frac{\ln 2}{2}} \Delta x_{1/e^2_{PSF}} = \sqrt{\frac{\ln 2}{2}} \cdot 2\omega_0 = \sqrt{\frac{\ln 2}{2}} \frac{2\lambda_0}{\pi} \left(\frac{f}{\omega_0'} \right) \\ &\cong \sqrt{\frac{\ln 2}{2}} \frac{2\lambda_0}{\pi} \left(\frac{1}{NA} \right). \end{aligned} \quad (2-34)$$

This is the least stringent criterion for the transverse resolution, *i.e.*, giving the highest resolution. Figure 2-23(b) shows the beam amplitude and intensity profile with relevant width corresponding to different criteria for transverse resolution with Gaussian beams. Figure 2-23(c) shows the transverse profiles in focus with limits for the resolution. $\Delta x_{FWHM_{PSF}}$ is shown in red. Alternative criteria for the transverse resolution, in order of increasing strictness, are: the $1/e$ diameter of the transverse PSF $\Delta x_{1/e_{PSF}} = \sqrt{\frac{1}{2}} \Delta x_{1/e^2_{PSF}}$ [26, 154], shown in yellow in Figure 2-23(c); the FWHM of the Gaussian beam illumination profile $\Delta x_{FWHM_{BeamAmplitude}} = \sqrt{\ln 2} \Delta x_{1/e^2_{PSF}}$ [10, 36], shown in green in Figure 2-23(c), and the $1/e^2$ of intensity (or PSF) beam diameter $\Delta x_{1/e^2_{PSF}} = 2\omega_0$, shown in blue in Figure 2-23(c).

When discussing system specification within the OCT community, resolution and FWHM transverse PSF width (or any of the other criteria) are used interchangeably without regard for the transverse profile of non-Gaussian beams (if used) and for the impact of scattering- and sample-induced aberration. This equivalence is valid in the absence of strong sidelobes when using different beams and in the absence of scattering- and sample-induced aberration due to reciprocity. This equivalence remains valid in this thesis, when using low-Fresnel number Bessel beams (see Section 3.1.3), and in the presence of scattering and sample-induced aberration, where the FWHM PSF width is unaffected for the tested imaging depths and scattering coefficient (see Section 6.2.2).

Depth of field (DOF)

The DOF of the OCT system is determined by the so-called confocal gating mechanism, which is equivalent to the axial PSF that would be obtained without coherence gating, shown in Figure 2-23(a). The DOF is usually defined, by reciprocity, as the full-width at half-maximum of the squared magnitude of the axial distribution of the focused electric field, *i.e.*, the illumination beam. That coincides with the depth over which the FWHM transverse resolution is $< \sqrt{2}$ of its value at focus, and is equal to twice the Rayleigh range, z_R , of the focused beam [36], *i.e.*,

$$DOF = 2z_R = \frac{2\pi n_g \omega_0^2}{\lambda_0} \cong n_g \frac{2\lambda_0}{\pi} \left(\frac{1}{NA^2} \right). \quad (2-35)$$

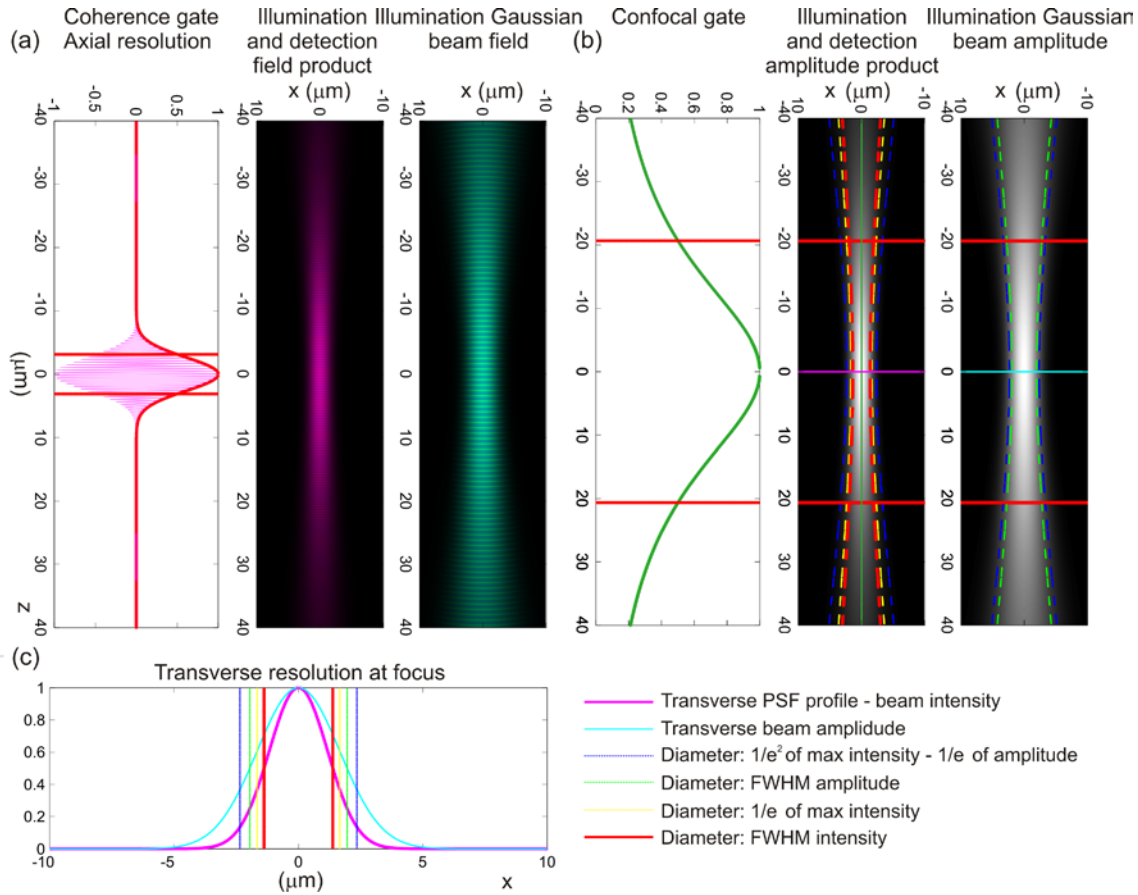


Figure 2-23. Schematic illustrating the determinants of resolution in OCT. (a) The coherence gate determines the axial resolution, as the FWHM of the axial PSF, shown in the left panel. The complex PSF (in absence of coherence gating) and the complex Gaussian beam are shown in the middle and right panels, respectively. (b) The axial depth of field, shown in the left panel, is the FWHM of the beam intensity axial profile (*i.e.*, axial PSF intensity in absence of coherence gating), shown in the middle panel, while the right panels shows the Gaussian beam amplitude. (c) Various criteria determining the transverse resolution.

The DOF is illustrated in the axial plot, bound by the red lines, in Figure 2-23(b). The DOF decreases quadratically with the beam NA, while the transverse resolution increases linearly with the beam NA. There is, thus, an inherent trade-off between achieving high transverse resolution, and having a large depth of field.

The latter is typically desirable, especially in FD-OCT, where a full A-scan is acquired at high speed without requiring moving parts. This requires objective lenses (and beams) with low numerical aperture, and limits the ability to exploit the high FD-OCT acquisition speed in microscopy applications [33]. One solution to this problem is the employment of beam shaping to increase the DOF without compromising the transverse resolution, as we shall see in Chapter 3.

The systems used in this thesis have beam NAs of ≈ 0.04 to 0.27 leading to transverse resolutions of 15 down to 1.5 μm and DOF (for Gaussian beams) of 335 down to 7.3 μm and axial resolutions, set by the source bandwidth, of 16 down to 1.5 μm . The OCT resolution defines an upper bound on the resolution of methods to measure elasticity using OCE.

2.3.2 OCT signal-to-noise ratio, sensitivity and contrast

The signal-to-noise ratio (SNR) is conventionally defined in terms of ratios of signal-to-noise electrical powers post-photodetection; an equivalent quantity may be defined in terms of the photocurrent in TD-OCT, given by [90]

$$SNR = \frac{\langle i_D^2(z) \rangle}{\sigma_{noise}^2}, \quad (2-36)$$

where the symbol $\langle \cdot \rangle$ represents the ensemble-average operation, σ_{noise}^2 represents the noise variance in units of squared current, A^2 , in the time (space) domain signal.

The sensitivity Σ of an OCT imaging system is defined as the minimum detectable reflectivity by the system, *i.e.*, the reflectivity yielding an $SNR = 1$ or, alternatively, the highest achievable signal-to-noise ratio [36]. Three noise sources limit OCT sensitivity: intensity (excess) noise, shot noise and receiver noise [36, 57, 90]. Stochastic fluctuations in the instantaneous source power are responsible for intensity noise, visible on the axial PSF in Figure 2-17. The quantised nature of light detection produces shot noise. In OCT, shot noise power is usually dominated by the reference arm power, not by the sample arm power, as is the case in non-interferometric systems. Electrical and thermal noise within the detector determine receiver noise. The relative contributions of intensity and receiver noise sources depends on the irradiance of the light incident on the detector [90]. Maximum sensitivity can, thus, be achieved by tuning the power returning from the reference arm [57, 90], as the reference reflectance is usually much greater than the sample reflectance for biological samples in OCT. This is shown in Figure 2-24, which plots the effects of these noise sources on the OCT sensitivity as a function of the reference arm reflectance.

OCT sensitivity is ultimately limited by shot noise, so systems operating at maximum sensitivity are said to be *operating in the shot-noise limit* or *shot-noise limited*.

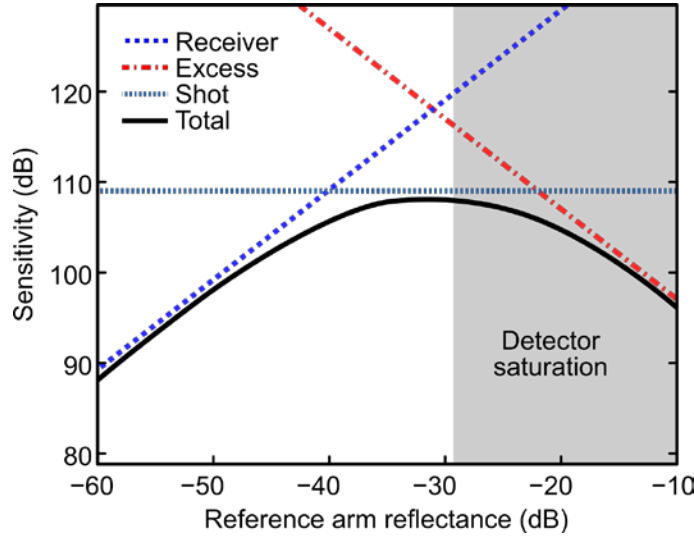


Figure 2-24. Calculated sensitivity for a typical spectrometer-based SD-OCT system. The maximum sensitivity is ultimately limited by the shot noise. Adapted from [57].

In the shot-noise limit, the sensitivity of TD-OCT is given by [155, 156],

$$\Sigma_{TD-OCT} = \frac{r_D P_S}{E_v B_W}, \quad (2-37)$$

where r_D is the responsivity of the detector, P_S is the optical power from the sample ($P_S \propto R_S$, the sample reflectivity), $E_v = h\nu$ is the photon energy (h is Planck's constant, ν is the optical frequency), and B_W is the low-pass electrical bandwidth of the detector. Since the axial resolution in OCT increases with bandwidth, there is a trade-off in TD-OCT between sensitivity and resolution.

By comparison, the shot-noise limited sensitivity of FD-OCT is [90, 91],

$$\Sigma_{FD-OCT} = \frac{r_D P_S \tau_i}{E_v} = \frac{r_D P_S M}{2 E_v B_W} \approx \frac{M}{2} \Sigma_{TD-OCT}, \quad (2-38)$$

where τ_i is the integration time of the detector, M is the number of pixels in the line-scan camera of the spectrometer in SD-OCT, or the equivalent number of spectral lines in the source for SS-OCT, $B_W/M = 1/2\tau_i$ by Nyquist's theorem [156]. This generally translates to a sensitivity advantage of 10 to 20 dB in favour of FD-OCT [57], which typically has a maximum sensitivity in the range 100 to 110 dB. In practice, the lower reflectances of most tissue samples mean the maximum SNR in an OCT image is typically in the range 30 to 50 dB [26].

We define OCT contrast [157] as the difference in dB between the square of the average OCT signal amplitude, $\overline{a_{D_{A1}}}^2$, in a homogeneous area $A1$ of a sample, and the

square of the average OCT signal amplitude, $\overline{a_{D_{A2}}}^2$, in a homogeneous area $A2$ neighbouring $A1$, near the border between the two:

$$C = 10\log_{10}(\overline{a_{D_{A1}}}^2) - 10\log_{10}(\overline{a_{D_{A2}}}^2). \quad (2-39)$$

However, since OCT is a coherent imaging modality, the measured signal amplitudes and SNR depend not only on the sample and reference reflectances, but will also be spatially modulated by speckle.

2.3.3 Speckle

Speckle is an intrinsic feature of images acquired with any imaging system employing coherent waves [158, 159]. The phenomenon is present and has been studied extensively in narrowband imaging modalities, such as ultrasound, astronomy, synthetic aperture radar and optical holography. It appears as a rapid fluctuation of the detected intensity (or field envelope) over the spatial extent of the image, conveying a granular texture.

In OCT [33], speckle is generated by the summation of multiple optical fields, backscattered from the sample arm of the interferometer. The fields must return to the detector within the temporal coherence gate, so that a coherent interference signal is generated with the light returning from the reference arm. They must also retain their spatial “coherence,” so that they are focused onto the optical detector (often via a confocal pinhole, or an optical fibre). They are represented by complex phasors, the sum of which determines the intensity and phase of the detected signal at a given depth in the sample. An OCT image of a human fingertip, clearly illustrating speckle, is presented in Figure 2-25.

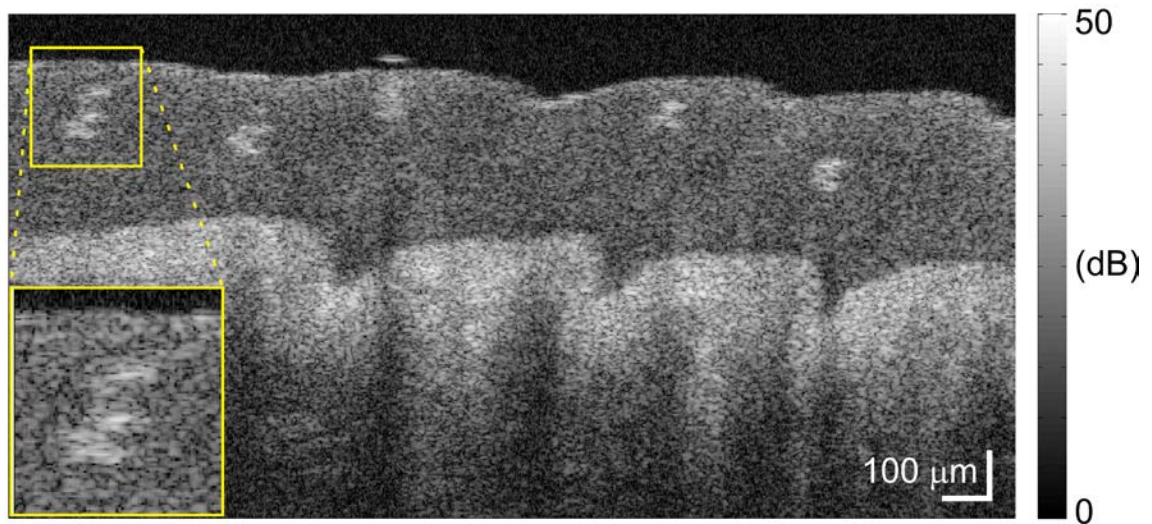


Figure 2-25. OCT image of a human fingertip with high contrast speckle pattern plotted on a logarithmic grayscale. The transverse extension of the image is 2 mm. Sweat duct extending from the papillary dermis to the *stratum corneum* highlighted in the inset.

Coherent, in the context of OCT, implies that the detected signal is linear with respect to the complex amplitude of the resultant back-propagating field. An imaging technique that is linear with the intensity (or the squared modulus of the complex amplitude) is termed *incoherent*. The large number of backscattered waves (treated as random variables) included in the summation at the detector leads to two very different results in the incoherent and coherent cases. In the incoherent case, where the fields are added on a positive intensity basis, the standard deviation of the sum will be much less than its mean, so the “random” fluctuations will be negligible. In the coherent case, where the fields are added on a complex amplitude basis, the mean will be zero, and the complex-valued fluctuations about it will constitute the entirety of the signal. (The fluctuations are preserved when the modulus of the signal is taken.) For this reason, speckle is present only in coherent techniques [158].

Although speckle is often regarded as a source of noise, it is distinct from system noise components such as intensity, shot, phase and electrical noises that depend only upon the properties of the source and detection scheme. In fact, its realization is highly sample dependent and time invariant, if the sample is stationary with respect to the probing beam. In this sense, speckle is fundamental to OCT image formation, to the extent that its complete removal would leave us with no image at all [160].

A specific speckle realization depends on the sample structure down to length scales on the order of fractions of the wavelength. Besides the sample structure or motion of its scattering components, the realization is also affected by the temporal and spatial characteristics of the light, multiple scattering and phase aberrations of the propagating beam and the aperture of the detector [160].

OCT speckle has been discussed in detail in the literature, *e.g.*, in [160-173], and in several reviews of the modality as a whole [10, 174, 175]. As in most of these cases speckle is perceived as a corrupting influence on the ability to resolve microstructure in the image, the majority of this literature is devoted to methods to suppress or overcome speckle. This often involves a form of ‘incoherent’ averaging of images of the same target featuring different speckle patterns (realizations), acquired with different system hardware configurations [160]. An alternative is to apply image post-processing techniques. In both cases, there is an inherent trade-off between the reduction in speckle contrast and the image resolution: ameliorating one comes at the expense of the other.

Another perspective is to regard speckle as a source of sample information and devise approaches to extract this information. In other areas of optical metrology [158, 159], such approaches are common. In considering its information content, a “missing frequency” characterisation of speckle [160, 176] is valuable. This interprets the phenomenon as arising

from the band-pass filtering properties of the OCT point-spread function. The speckled OCT signal is a reconstruction of only a small subset of the entire range of sample spatial frequencies; speckle only conveys information in the specific frequency range. If described in statistical terms, it is possible in some instances to extract sample-dependent information from the speckle's temporal or spatial characteristics. Dynamic speckle is also used to determine tissue motion, by speckle tracking or cross-correlation methods, and finds application in functional imaging such as OCE [166, 177], measuring displacement resulting from compression introduced to the sample to extract a local strain map of the sample, and micro-angiography [178], quantifying blood flow.

2.3.4 Elastogram quality

Sources of noise in phase-sensitive optical coherence elastography

In phase-sensitive optical coherence elastography, the elastography technique we use in this thesis, image quality is strongly affected by the noise sources in the OCT phase difference measurements.

Noise sources in phase-sensitive OCE depend mainly on the OCT SNR and the amount of strain and displacement the sample is subject to between consecutive OCT images, at any given pixel in the phase difference image. Displacements deriving from a phase change of greater than $\pm\pi$ are ambiguous. This is a limitation referred to as *phase wrapping* [179] and sets the upper limit of measurable phase difference, if phase unwrapping algorithms are not used, otherwise the limitation is set by *phase decorrelation*, as described in the Section 7.2.2.

One fundamental limitation on the minimum detectable phase difference arises from the OCT SNR of a measurement. To quantify this effect, in [180], 1024 consecutive depth profiles (A-scans) at a single point on a glass slide were obtained at different SNRs using a variable neutral density filter in the sample arm. The phase difference between the front and back surfaces of the glass slide was determined, and the standard deviation of these phase differences was calculated. This standard deviation directly yields the minimum detectable phase difference. The resulting standard deviations demonstrate a decreasing minimum detectable phase difference, $\Delta\phi_m$, with increasing SNR. In the shot noise limit, noise can be modelled as a random vector, \mathbf{A}_n , added to a complex vector, \mathbf{A}_s , describing light returning from the sample, to yield a measured complex quantity, \mathbf{A}_m .

This case corresponds to the case modelled by a random phasor sum \mathbf{A}_n plus a known constant phasor \mathbf{A}_s [34]. The modulus $|\mathbf{A}_m|$ will be Rician-distributed with parameters $|\mathbf{A}_s|$, and σ , where σ is the noise standard deviation [26].

Figure 2-26 shows the marginal probability density function $p_\phi(\phi)$ for the OCT signal phase, for a range of parameter ratios.

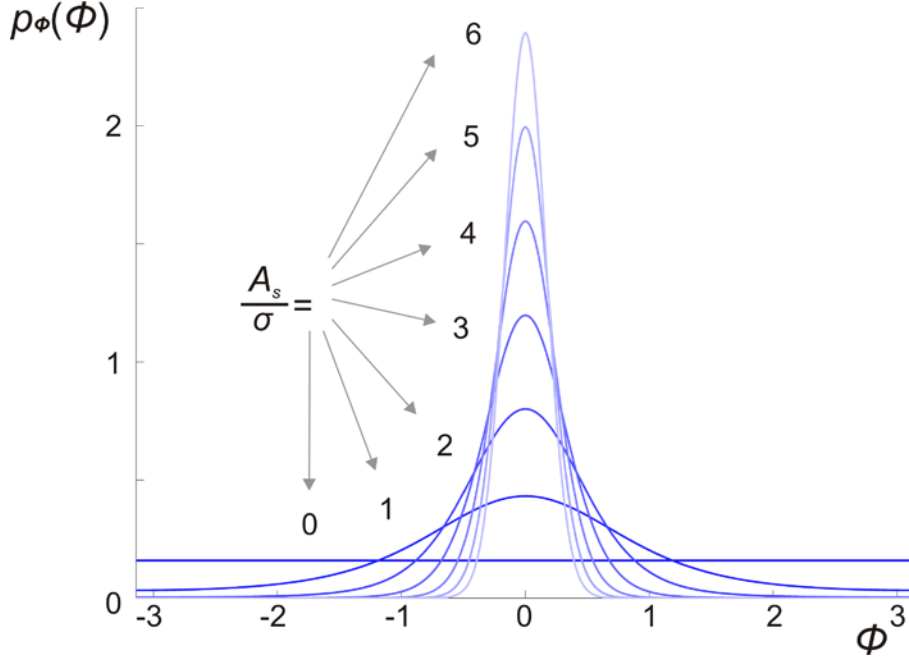


Figure 2-26. Marginal probability density function $p_\phi(\phi)$ for the OCT signal phase. Adapted from [34].

The SNR of the glass slide measurement is given by $\text{SNR} = (|\mathbf{A}_s|/|\mathbf{A}_n|)^2$. Assuming a good SNR ($|\mathbf{A}_n| \ll |\mathbf{A}_s|$), the standard deviation of the phase ϕ_m of \mathbf{A}_m is given by $\sigma_{\phi_m}^2 = \frac{1}{2}(|\mathbf{A}_n|/|\mathbf{A}_s|) = \frac{1}{2}(\text{SNR})^{-1}$. The minimum detectable phase difference $\sigma_{\Delta\phi_m}$ between two measured phases ϕ_m can now be determined as:

$$\sigma_{\Delta\phi_m} = \sqrt{2\sigma_{\phi_m}^2} = (\text{SNR})^{-\frac{1}{2}}. \quad (2-40)$$

Eq. (2-40) indicates that low OCT SNR is a fundamental noise factor affecting the precision of OCE, *i.e.*, the repeatability of the tissue displacement and strain measurement. Using a WLS linear regression over a sliding window on the measured axial displacement, with the weights being the OCT SNR at any given depth [106], allows for a more precise strain estimation in phase-sensitive OCE.

In this thesis, we consider the precision of OCE as quantified by three metrics: displacement sensitivity, strain sensitivity, and strain SNR, as further defined in Section 7.2.2.

2.4 Conclusion

In this chapter, we introduced the basics and working principles of low-coherence interferometry, optical coherence tomography and optical coherence elastography. We overviewed their uses in various biomedical fields and we have defined the descriptors of image quality in both imaging modalities.

This provides the background necessary in this thesis to understand the research aimed at quantifying and improving image quality by means of beam shaping and image formation simulations, which forms the remainder of this dissertation.

The next chapter will deal with beam shaping techniques and Bessel beam generation and characterisation, as one of the means used to improve image quality.